









Low Gilbert damping and high thermal stability of Ru-seeded $L1_0$ -phase FePd perpendicular magnetic thin films at elevated temperatures **F**

Cite as: Appl. Phys. Lett. **117**, 082405 (2020); <https://doi.org/10.1063/5.0016100>

Submitted: 01 June 2020 . Accepted: 04 August 2020 . Published Online: 25 August 2020

Delin Zhang , Dingbin Huang , Ryan J. Wu, Dustin Lattery , Jinming Liu , Xinjun Wang, Daniel B. Gopman , K. Andre Mkhoyan , Jian-Ping Wang , and Xiaojia Wang 

COLLECTIONS

F This paper was selected as Featured



View Online



Export Citation



CrossMark

ARTICLES YOU MAY BE INTERESTED IN

[Concurrent magneto-optical imaging and magneto-transport readout of electrical switching of insulating antiferromagnetic thin films](#)

Applied Physics Letters **117**, 082401 (2020); <https://doi.org/10.1063/5.0011852>

[Enhancement of the spin-orbit torque efficiency in W/Cu/CoFeB heterostructures via interface engineering](#)

Applied Physics Letters **117**, 082409 (2020); <https://doi.org/10.1063/5.0015557>

[Evolution of strong second-order magnetic anisotropy in Pt/Co/MgO trilayers by post-annealing](#)

Applied Physics Letters **117**, 082403 (2020); <https://doi.org/10.1063/5.0018924>

Lock-in Amplifiers
up to 600 MHz



Low Gilbert damping and high thermal stability of Ru-seeded L1₀-phase FePd perpendicular magnetic thin films at elevated temperatures

Cite as: Appl. Phys. Lett. **117**, 082405 (2020); doi: [10.1063/5.0016100](https://doi.org/10.1063/5.0016100)

Submitted: 1 June 2020 · Accepted: 4 August 2020 ·

Published Online: 25 August 2020 · Corrected: 26 August 2020



View Online



Export Citation



CrossMark

Delin Zhang,^{1,a)}  Dingbin Huang,²  Ryan J. Wu,³  Dustin Lattery,²  Jinming Liu,¹  Xinjun Wang,^{1,4}  Daniel B. Gopman,⁴  K. Andre Mkhoyan,³  Jian-Ping Wang,¹  and Xiaojia Wang^{2,a)} 

AFFILIATIONS

¹Electrical and Computer Engineering, University of Minnesota, Minneapolis, Minnesota 55455, USA

²Department of Mechanical Engineering, University of Minnesota, Minneapolis, Minnesota 55455, USA

³Chemical Engineering and Materials Science, University of Minnesota, Minneapolis, Minnesota 55455, USA

⁴Materials Science and Engineering Division, National Institute of Standards and Technology, Gaithersburg, Maryland 20899, USA

^{a)}Authors to whom correspondence should be addressed: dizhang@umn.edu and wang4940@umn.edu

ABSTRACT

Bulk perpendicular magnetic anisotropy materials are proposed to be a promising candidate for next-generation ultrahigh density and ultra-low energy-consumption spintronic devices. In this work, we experimentally investigate the structure, thermal stability, and magnetic properties of FePd thin films seeded by an Ru layer. An *fcc*-phase Ru layer induces the highly-ordered L1₀-phase FePd thin films with perpendicular magnetic anisotropy ($K_u \sim 10.1$ Merg/cm³). The thermal stability of FePd samples is then studied through the annealing process. It is found that a $K_u \sim 6.8$ Merg/cm³ can be obtained with an annealing temperature of 500 °C. In addition, the Gilbert damping constant α , an important parameter for switching current density, is determined as a function of the testing temperature. We observe that α increases from 0.006 to 0.009 for the as-deposited FePd sample and from 0.006 to 0.012 for the 400 °C-annealed FePd sample as the testing temperature changes from 25 °C to 150 °C. These results suggest that Ru-seeded FePd provides great potential in scaling perpendicular magnetic tunnel junctions below 10 nm for applications in ultralow energy-consumption spintronic devices.

Published under license by AIP Publishing. <https://doi.org/10.1063/5.0016100>

As the key building block of magnetic random-access memory (MRAM), perpendicular magnetic tunnel junctions (p-MTJs) have been extensively investigated.^{1–8} For MRAM, when scaling MTJ devices to commercially sustainable sizes, like 10-nm nodes, a large perpendicular magnetic anisotropy (PMA, K_u) and a low damping constant (α) for ferromagnetic materials are required to realize longer retention time and ultralow switching current density. Meanwhile, to satisfy the requirement of an existing back-end-of-line CMOS process, the ferromagnetic materials are required to maintain the magnetic properties under a high-temperature thermal treatment process (e.g., the annealing temperature, $T_{\text{ann}} > 400$ °C).⁹ In addition, the memory and logic devices must maintain high performance in extreme environments for special applications, including automotive, military, and aerospace. This demand requires the devices to be able to operate at elevated temperatures (~ 125 °C).¹⁰

Recently, bulk PMA L1₀-phase FePd has attracted considerable interest for developing ultrahigh-density and ultralow-energy memory

and logic devices due to its large K_u , low α , high thermal stability (Δ), scalability, and theoretically low switching current density.^{11–18} These properties of L1₀-phase FePd also depend on the growth conditions, such as the seed layer and the thermal treatment process. So far, many materials have been used as a seed layer to develop FePd PMA thin films, like Cr/Pd^{12,14–16} and Cr/Pt.^{17,18} Although the Cr/Pd and Cr/Pt seed layers can induce the high-quality FePd thin film because of a small lattice mismatch with FePd, the interdiffusion could change the composition of FePd with the high-temperature thermal treatment process, which can change PMA and α , particularly detrimental for ultrathin films in p-MTJs. Therefore, exploring the seed layer to grow high-performance FePd thin films will be crucial for realizing the high performance and CMOS-compatible spin memory devices. As a seed layer, the spacer or capping layer, the hexagonal close-packed (*hcp*)-phase ruthenium (Ru) has been used for spintronic device applications^{19–24} for more than three decades. It is also theoretically predicted that Ru can form an *fcc*-phase²⁵ but has not been experimentally

realized until recently when we demonstrated an *fcc*-phase Ru layer as a spacer layer.¹⁸ We find that *fcc*-phase Ru has a very small lattice mismatch (less than 1%) with FePd, also *fcc*-phase Ru induces a large interlayer exchange coupling in the FePd/Ru/FePd synthetic antiferromagnetic structure.

In this work, we investigate the crystalline structure, thermal stability, and magnetic properties of the FePd thin films seeded by an *fcc*-phase Ru layer. The (001) textured growth of Ru and FePd layers is first confirmed through XRD and STEM characterizations. Then FePd samples are annealed up to 500 °C to identify the thermal endurance of these materials. The magnetization dynamics of the as-deposited and annealed samples were measured with the ultrafast time-resolved magneto-optical Kerr effect (TR-MOKE) metrology to extract the Gilbert damping constant, α . This parameter is important for evaluating the switching current density for the operation of MTJ devices built upon this material. Furthermore, we study α as a function of the testing temperature from the room temperature (RT) (25 °C) to 150 °C. Our results suggest that Ru-seeded L1₀-phase FePd can maintain a relatively small α for the temperatures ranging from 25 °C up to 150 °C, indicating the thermal robustness of FePd thin films will be beneficial for ultralow energy-consumption spintronic applications across a wide temperature range.

The FePd samples were grown on (001) MgO single-crystal substrates with a Cr/Ru seed layer in an ultrahigh vacuum magnetron sputtering system with a base pressure less than 5.0×10^{-8} Torr. During the deposition of the Cr (15 nm)/Ru (5 nm) seed layer and FePd layer, the substrate temperature was kept at 350 °C. The pressure of Ar working gas was 4.5 mTorr for the FePd layer and 2.0 mTorr for the other layers. The 7.5-nm FePd thin films were prepared by co-sputtering with the Fe and Pd targets. A 5-nm-thick Ta capping layer was grown at room temperature (RT). The FePd thin films with a Cr (15 nm)/Pt (5 nm) seed layer were also grown for comparison with the same experimental condition of the Cr/Ru seed layer. The magnetic properties were measured with the Vibrating Sample Magnetometer (VSM) module of a Physical Property Measurement System (PPMS). The structural features of FePd thin films were characterized by out-of-plane (θ - 2θ scan) x-ray diffraction (XRD) with Cu-K α radiation ($\lambda = 0.15418$ nm) using a Bruker D8 Discover system and by scanning transmission electron microscopy (STEM) using aberration-corrected FEI Titan G2 60–300 STEM. Cross section samples for STEM study were prepared by using a Zeiss Auriga focused-ion beam (FIB) system. Energy-dispersive x-ray spectroscopy (EDS) signal was acquired by scanning the electron probe across the sample area continuously for 25 min at ~ 200 pA electron beam current. The α value of the Ru-seeded FePd thin films was measured by the TR-MOKE and the ferromagnetic resonance (FMR) methods.^{16,26–28} For TR-MOKE measurements conducted in this study, a $10\times$ objective lens was used to focus the laser beams onto the sample surface, which produced a $1/e^2$ beam spot size of $w_0 \approx 6 \mu\text{m}$. The pump and probe fluences were set as ~ 0.2 and $0.1 \text{ mJ}/\text{cm}^2$, respectively. An external magnetic field (H_{ext}) of up to 20 kOe was applied to the sample at an angle of θ_H with respect to the sample surface normal.

The *fcc*-phase Ru with the lattice parameter of $a = b = c = 0.383$ nm (Ref. 18) has a small lattice mismatch ($\sim 0.5\%$) with L1₀-phase FePd ($a = b = 0.385$ nm, $c = 0.372$ nm).²⁹ It can induce the highly ordered L1₀-phase FePd following a textured growth like Pt and Pd, as shown in Fig. 1(a). The crystalline structures of Ru-seeded

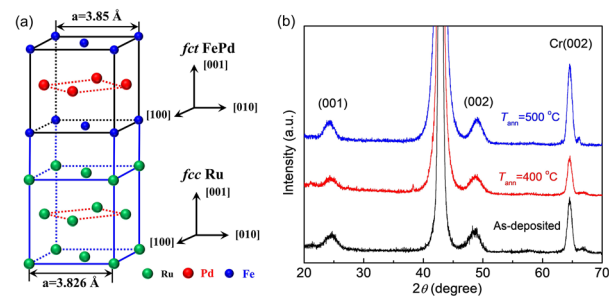


FIG. 1. (a) Schematic of the epitaxial relationship between *fcc*-phase Ru and *fct*-phase FePd. The lattice mismatch between FePd and Ru is less than 1.0%. (b) The out-of-plane (θ - 2θ scans) XRD patterns as a function of the annealing temperatures for Ru-seeded FePd thin films. The very clear (001) and (002) peaks of the L1₀-phase are observed, indicating the high-ordered FePd thin films.

and Pt-seeded FePd samples characterized with XRD are shown in Figs. 1(b) and S1. For the Ru-seeded FePd thin film, the (001) and (002) peaks are clearly visible with the different annealing temperatures (T_{ann}), suggesting a well-formed superlattice structure. It is also found that the intensity of the (001) peak is enhanced with the increase in T_{ann} , indicating that the annealing process facilitates the crystallization of the Ru-seeded FePd sample. Meanwhile, we do not notice any apparent peak shift, indicating that the lattice of Ru-seeded FePd is not changed during the annealing processes at high temperatures of up to 500 °C. While for Pt-seeded FePd, although the (001) peak can also be observed, the (002) peak merges with the (200) peak of the Pt seed layer with the increase in T_{ann} . The intensity of the (001) peak decreases and the peak shifts to a smaller angle (Fig. S1 in the [supplementary material](#)), implying that the Pt atoms diffuse into FePd and change the lattice and composition of the FePd sample. In addition, the ordering parameter (S) of Ru-seeded and Pt-seeded FePd samples is calculated based on the equation $S^2 = [I(001)/I(002)]/[I_{\text{cal}}(001)/I_{\text{cal}}(002)]$, where I and I_{cal} are the measured integrated intensity and the calculated intensity. The term of $I_{\text{cal}}(001)/I_{\text{cal}}(002)$ is obtained from the equation $I_{\text{cal}}(001)/I_{\text{cal}}(002) = (|F_{001}|^2 L_{001} A_{001})/(|F_{002}|^2 L_{002} A_{002})$, where F , L , and A are the structural, Lorentz, and absorption factors, respectively.³⁰ The S values of the as-deposited, 400 °C-annealed, and 500 °C-annealed samples are 0.79, 0.82, and 0.86 for Ru-seeded FePd, and are 0.94, 0.70, and 0.62 for Pt-seeded FePd, respectively. The results indicate that the annealing process enhances the crystallinity of Ru-seeded FePd samples but damages the crystallinity of the Pt-seeded FePd samples, which agrees with the variation trend of the sample magnetic properties.

To confirm the epitaxial relationship between the Ru and FePd layers, the as-deposited Ru-seeded FePd thin film was thinned into an electron-transparent lamella (~ 50 nm thick) using FIB and, subsequently, inserted into STEM for characterization. Figure 2(a) shows the high-angle annular dark-field (HAADF) STEM images of the sample in cross section, where the (001) epitaxial relationship can be observed throughout the stack. As can be seen, the (001) textured Ru layer is following the Cr seed-layer grown on the (001)-oriented MgO substrate. Then, FePd takes the Ru texture and forms the high-quality L1₀-phase. The elemental compositions of these crystalline layers were determined by using energy dispersive x-ray (EDX) spectroscopy obtained in STEM along with HAADF images, as shown in

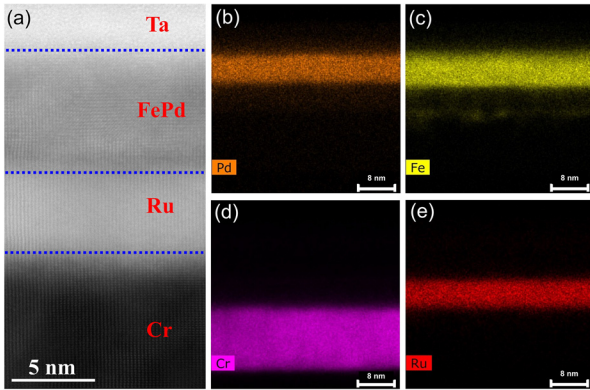


FIG. 2. (a) Atomic-resolution HAADF-STEM image of the as-deposited Ru-seeded FePd thin film. (b)–(e) STEM-EDX elemental maps of Cr, Ru, Pd, Fe, and Ta obtained from the same layer stack.

Figs. 2(b)–2(e). While Cr/Ru interface is compositionally sharp, a slight diffusion at the FePd/Ru interface as well as a slight accumulation of Fe at the Cr/Ru interface are observed by comparing the STEM-EDX images of Figs. 2(b) and 2(c), which are likely due to the high-temperature deposition.

The magnetic properties vs T_{ann} of the FePd thin films were characterized with the VSM module of a PPMS. The magnetic hysteresis (M - H) loops of Ru-seeded and Pt-seeded FePd thin films are plotted in Figs. 3(a)–3(c) and Fig. S2(a) in the supplementary material, respectively. It is clearly shown that the PMA of Ru-seeded FePd is enhanced relative to Pt-seeded FePd thin films with the increase in T_{ann} . For Ru-seeded samples, the out-of-plane M - H loop maintains high squareness and remanence while the in-plane M - H loop gradually narrowed with increased T_{ann} up to 500 °C. However, a 500 °C annealing treatment causes Pt-seeded FePd thin films to lose the square shape of the out-of-plane loops. Their remanence decreases and the in-plane component of magnetization increases, suggesting that the perpendicular anisotropy is reduced when T_{ann} approaches 500 °C. It is also obvious that the effective perpendicular magnetic anisotropy field ($H_{k,\text{eff}}$) value

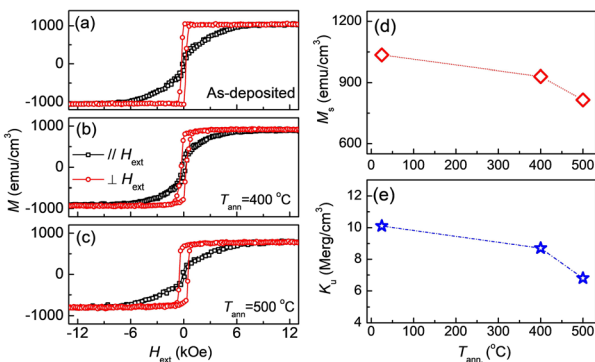


FIG. 3. (a)–(c) The RT magnetization hysteresis (M - H) loops of Ru-seeded FePd as a function of the annealing temperatures, (d) magnetization (M_s), and (e) magnetic anisotropy (K_u) as a function of the annealing temperatures of FePd samples. With the increase in the annealing temperature, the M_s and K_u values decrease, implying the interfacial diffusion but still larger enough for the device application.

obtained from M - H loops slightly increases for Ru-seeded FePd but decreases from 8 kOe to 4 kOe for Pt-seeded FePd. Meanwhile, the saturation magnetization (M_s) and K_u can be calculated based on the M - H loop measurement for both seed layers. The results are plotted in Figs. 3(d) and 3(e) and Figs. S2(b) and S2(c) in the supplementary material. It is clearly observed that the M_s and K_u values decrease with the increases of the annealing temperatures. For Ru-seeded FePd, M_s decreases from 1030 emu/cm³ to 815 emu/cm³ and K_u decreases from ~10.1 Merg/cm³ to ~6.8 Merg/cm³. Pt-seeded FePd shows a more accelerated decline with the increase in T_{ann} , for which M_s and K_u decrease from 1050 emu/cm³ to 750 emu/cm³ and from ~11.5 Merg/cm³ to ~5.0 Merg/cm³, respectively. Based on these results, we find that there is an interdiffusion for both two samples at a high annealing temperature. However, Ru-seeded samples show better annealing performance than that of Pt-seeded samples. This is likely because the Ru is inactive compared to Pt, thus less Ru diffuses into FePd. Meanwhile, when Ru diffuses into the FePd thin film, it prefers to form the alloy with Fe not Pd since Pd and Ru are immiscible,^{31,32} like Cu addition.^{33,34} However, Pt diffuses into FePd and occupies the Pd sites, leading to the formation of the Fe_{1-x}(PdPt)_x alloy. This changes the composition of thin films, which subsequently causes a change in the magnetic properties.³⁵

The α value of FePd thin films is extracted from TR-MOKE measurements. A schematic of the sample configuration for TR-MOKE measurements is shown in Fig. 4(a). The TR-MOKE signal is fitted by²⁸

$$\theta_K = A + Be^{-t/C} + D \sin(2\pi ft + \varphi)e^{-t/\tau}, \quad (1)$$

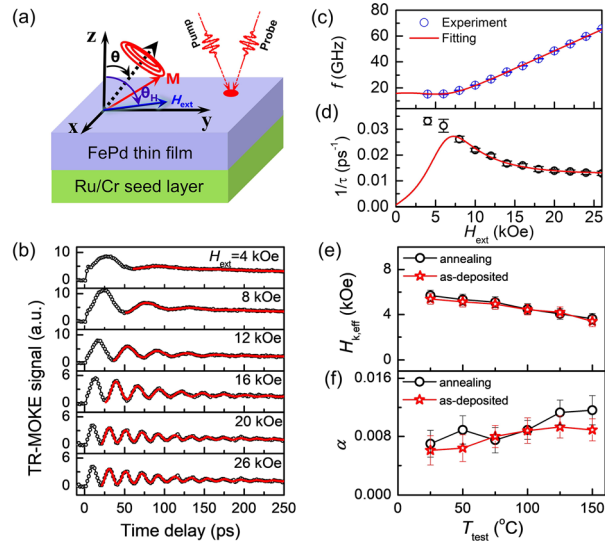


FIG. 4. (a) The schematic of the sample configuration for TR-MOKE measurements. (b) RT TR-MOKE data (symbols) and model fitting (solid curves) of the 400 °C-annealed sample. TR-MOKE measurements were carried out at $\theta_H \approx 80^\circ$ for varying H_{ext} from 4.0 to 20.0 kOe. (c) and (d) Representative example of the fitting of f vs H_{ext} and $1/\tau$ vs H_{ext} for the 400 °C-annealed sample. (e) and (f) The temperature-dependent effective anisotropic field ($H_{k,\text{eff}}$) and Gilbert damping constant (α) extracted from TR-MOKE measurements for both as-deposited and 400 °C-annealed samples.

where θ_K denotes the Kerr signal. The first two terms in the right-handed side represent the thermal background, which are characterized by the offset (A), amplitude (B), and exponential decaying constant (C). The third term is related to the precession with f , τ , D , and φ denoting, respectively, the precession frequency, relaxation time, amplitude, and phase shift.

The dependence of f and τ on H_{ext} can be obtained through the Smit–Suhl approach, based on the Landau–Lifshitz–Gilbert equation, as shown by the following equations:^{13,28}

$$f = \frac{\gamma}{2\pi} \sqrt{H_1 H_2}, \quad (2)$$

$$H_1 = H_{\text{ext}} \cos(\theta - \theta_H) + H_{k,\text{eff}} \cos^2(\theta), \quad (3)$$

$$H_2 = H_{\text{ext}} \cos(\theta - \theta_H) + H_{k,\text{eff}} \cos(2\theta), \quad (4)$$

$$2H_{\text{ext}} \sin(\theta_H - \theta) = H_{k,\text{eff}} \sin(2\theta), \quad (5)$$

$$\frac{1}{\tau} = \frac{1}{2} \alpha \gamma (H_1 + H_2) + \pi \left| \frac{df}{dH_{k,\text{eff}}} \right| \Delta H_{k,\text{eff}} + \pi \left| \frac{df}{d\theta_H} \right| \Delta \theta_H, \quad (6)$$

where γ is the gyromagnetic ratio, θ is the equilibrium angle of the magnetization [see Fig. 4(a)], and $H_{k,\text{eff}}$ denotes the effective anisotropy field. The second and third terms on the right-handed side of Eq. (6) take into account the inhomogeneous broadening resulting from the distributions of the effective anisotropy field ($\Delta H_{k,\text{eff}}$) and the easy axis ($\Delta \theta_H$).¹⁶

To investigate the temperature dependence of α , the as-deposited and 400 °C-annealed Ru-seeded FePd thin films were measured at temperatures ranging from 25 °C to 150 °C. For these measurements, H_{ext} was set at $\theta_H \approx 80^\circ$ and varied from 4 kOe to 20 kOe. Figure 4(b) depicts the RT TR-MOKE signals (symbols) and the model fitting of θ_K (red lines) as functions of time delay for the 400 °C-annealed Ru-seeded FePd thin film. A complete set of TR-MOKE raw data are shown in Fig. S3 of the supplementary material. A damped magnetization precession is clearly observed, resulting from laser excitation. The measured values of f as a function of H_{ext} at RT can be fitted to Eq. (2) by treating γ , θ_H , and $H_{k,\text{eff}}$ as the fitting parameters, as shown in Fig. 4(c). In Fig. 4(d), the $1/\tau$ measured at RT as a function of H_{ext} is fitted by Eq. (6) to extract the values of intrinsic α . Only the data at a relatively high H_{ext} ($H_{\text{ext}} \geq 2H_{k,\text{eff}}$) are used to promote coherent magnetization precession and thus suppress the inhomogeneous broadening and two-magnon scattering contributions. More details about the fitting of f and $1/\tau$ as functions of H_{ext} at different temperatures are illustrated in Fig. S4 of the supplementary material for both the as-deposited and 400 °C-annealed samples.

Figures 4(e) and 4(f) show the temperature dependence of $H_{k,\text{eff}}$ and α obtained from TR-MOKE measurements for both as-deposited and 400 °C-annealed samples. There exists an apparent decreasing trend of $H_{k,\text{eff}}$ (from ~ 5.7 kOe to ~ 3.6 kOe) for both samples when the testing temperature (T_{test}) increases from 25 °C to 150 °C, as shown in Fig. 4(e). This means that K_u decreases with the increase in T_{test} . Following the equation of the thermal stability $\Delta = \frac{K_u V}{k_B T} = \frac{K_u (A t_{\text{FM}})}{k_B T}$ (where A is the area of the MTJ pillar and t_{FM} is the thickness of the ferromagnetic free layer),³⁶ it is noted that the Δ value will decrease with the increase in T_{test} . For bulk PMA FePd, we can easily increase t_{FM} to remain the large Δ value and make the MTJ device thermal stable at the high operation temperature. However, for interfacial PMA materials (e.g., Ta/CoFeB/MgO³ or W/CoFeB/MgO²⁸), there

is no space to tune the Δ value because the thickness of the CoFeB layer is limited to less than 1.5 nm. The RT values of α for the as-deposited and 400 °C-annealed samples are extracted to be 0.006. These values are nearly half of the values reported for the Ta/CoFeB/MgO and W/CoFeB/MgO stacks in prior studies.^{1,28} Meanwhile, to cross-check the values of α for Ru-seeded FePd thin film, we measure α using FMR for the as-deposited FePd samples. The results are provided in Figs. S5(a) and S5(b) of the supplementary material. The value of α extracted from FMR is 0.0086 ± 0.0005 , on par with the value obtained from TR-MOKE within the uncertainty. Furthermore, we conduct TR-MOKE measurements to obtain temperature-dependent α by varying T_{test} from 25 °C to 150 °C. The results are plotted in Fig. 4(f) for the as-deposited and 400 °C-annealed samples. It is found that when T_{test} changes from RT to 150 °C, α increases slightly for both samples: from 0.006 to 0.009 for the as-deposited FePd thin film and from 0.006 to 0.012 for the 400 °C-annealed FePd thin film. The values are lower than that of the interfacial PMA stacks [e.g., Ta/CoFeB/MgO (~ 0.02), W/CoFeB/MgO (~ 0.015)]. These results suggest the great promise of Ru-seeded L1₀-FePd as building blocks for low energy-consumption MTJ devices because a small α can dramatically reduce the switching current.³⁷ Normally, α originates from the contributions of spin orbital coupling (SOC) and electron–phonon interaction,³⁸ and thus, α is mainly dependent on the structure and crystallinity of magnetic materials. It is found that α of FePd is mainly dependent on its S , not the thickness (e.g., α decreases with the increase in the S values).^{13,16} However, other effects could also influence α , such as spin pumping,^{39,40} the epitaxial strain between the ferromagnet and substrate, and the element impurity due to the diffusion from the seed and/or capping layers during post-annealing.^{13,16}

In conclusion, through the characterizations of the crystalline structure, thermal stability, and magnetic properties, we find that Ru seed layer plays a critical role in enhancing the PMA and thermal stability of the FePd thin films compared to the Pt seed layer. The Ru-seeded FePd thin film can retain the good magnetic properties after 400 °C annealing with $K_u \sim 8.7$ Merg/cm³ and $\alpha \sim 0.006$, which can keep the MTJ devices thermal stable with much better performance than that of the interfacial PMA thin films. It is also found that α show a slight increase from 0.006 to 0.009 for the as-deposited FePd sample and from 0.006 to 0.012 for the 400 °C-annealed FePd sample, respectively, when the testing temperature increases from 25 °C to 150 °C. Such small change of α will be beneficial for switching the MTJ devices with a low critical current density during the operation process.

See the supplementary material for additional results about the magnetic property, structural characterization, TR-MOKE, and FMR of Pt-seeded and Ru-seeded FePd samples.

This work was supported in part by the Defense Advanced Research Projects Agency (DARPA) No. HR001117S0056-FP-042 “Advanced MTJs for computation in and near random access memory,” by the ASCENT, one of the six centres in JUMP, a Semiconductor Research Corporation program, sponsored by MARCO and DARPA, by the National Institute of Standards and Technology, and by the Advanced Storage Research Consortium (ASRC). Parts of the work were carried out in the Characterization Facility of the University of Minnesota, which receives partial support from NSF through the MRSEC program (No. DMR-1420013).

DATA AVAILABILITY

The data that support the findings of this study are available within the article and its [supplementary material](#).

REFERENCES

- ¹S. Ikeda, K. Miura, H. Yamamoto, K. Mizunuma, H. D. Gan, M. Endo, S. Kanai, J. Hayakawa, F. Matsukura, and H. Ohno, *Nat. Mater.* **9**, 721–724 (2010).
- ²P. Khalili Amiri, Z. M. Zeng, J. Langer, H. Zhao, G. Rowlands, Y.-J. Chen, I. N. Krivorotov, J.-P. Wang, H. W. Jiang, J. A. Katine, Y. Huai, K. Galatsis, and K. L. Wang, *Appl. Phys. Lett.* **98**, 112507 (2011).
- ³M. Gajek, J. J. Nowak, J. Z. Sun, P. L. Trouilloud, E. J. O Sullivan, D. W. Abraham, M. C. Gaidis, G. Hu, S. Brown, Y. Zhu, R. P. Robertazzi, W. J. Gallagher, and D. C. Worledge, *Appl. Phys. Lett.* **100**, 132408 (2012).
- ⁴L. Thomas, G. Jan, J. Zhu, H. Liu, Y.-J. Lee, S. Le, R.-Y. Tong, K. Pi, Y.-J. Wang, D. Shen, R. He, J. Haq, J. Teng, V. Lam, K. Huang, T. Zhong, T. Torng, and P.-K. Wang, *J. Appl. Phys.* **115**, 172615 (2014).
- ⁵G. Hu, J. H. Lee, J. J. Nowak, J. Z. Sun, J. Harms, A. Annunziata, S. Brown, W. Chen, Y. H. Kim, G. Lauer, L. Liu, N. Marchack, S. Murthy, E. J. O'Sullivan, J. H. Park, M. Reuter, R. P. Robertazzi, P. L. Trouilloud, Y. Zhu, and D. C. Worledge, in *Proceedings of the International Electron Devices Meeting Digest* (2015), pp. 26.3.1–26.3.4.
- ⁶A. D. Kent and D. C. Worledge, *Nat. Nanotechnol.* **10**, 187–191 (2015).
- ⁷B. Dieny and M. Chshiev, *Rev. Mod. Phys.* **89**, 025008 (2017).
- ⁸S. Bhatti, R. Sbiaa, A. Hirohata, H. Ohno, S. Fukami, and S. N. Piramanayagam, *Mater. Today* **20**, 530–548 (2017).
- ⁹A. J. Annunziata, P. L. Trouilloud, S. Bandiera, S. L. Brown, E. Gapihan, E. J. O Sullivan, and D. C. Worledge, *J. Appl. Phys.* **117**, 17B739 (2015).
- ¹⁰D. Apalkov, B. Dieny, and J. M. Slaughter, *Proc. IEEE* **104**, 1796–1830 (2016).
- ¹¹M. Weisheit, S. Fähler, A. Marty, Y. Souche, C. Poinignon, and D. Givord, *Science* **315**, 349–351 (2007).
- ¹²F. Bonell, S. Murakami, Y. Shiota, T. Nozaki, T. Shinjo, and Y. Suzuki, *Appl. Phys. Lett.* **98**, 232510 (2011).
- ¹³S. Iihama, A. Sakuma, H. Naganuma, M. Oogane, T. Miyazaki, S. Mizukami, and Y. Ando, *Appl. Phys. Lett.* **105**, 142403 (2014).
- ¹⁴H. Naganuma, G. Kim, Y. Kawada, N. Inami, K. Hatakeyama, S. Iihama, K. M. N. Islam, M. Oogane, S. Mizukami, and Y. Ando, *Nano Lett.* **15**, 623–628 (2015).
- ¹⁵H.-R. Lee, K. Lee, J. Cho, Y.-H. Choi, C.-Y. You, M.-H. Jung, F. Bonell, Y. Shiota, S. Miwa, and Y. Suzuki, *Sci. Rep.* **4**, 6548 (2015).
- ¹⁶S. Iihama, A. Sakuma, H. Naganuma, M. Oogane, S. Mizukami, and Y. Ando, *Phys. Rev. B* **94**, 174425 (2016).
- ¹⁷D.-L. Zhang, K. B. Schliep, R. J. Wu, P. Quarterman, D. R. Hickey, Y. Lv, X. Chao, H. Li, J.-Y. Chen, Z. Zhao, M. Jamali, K. A. Mkhoyan, and J.-P. Wang, *Appl. Phys. Lett.* **112**, 152401 (2018).
- ¹⁸D.-L. Zhang, C. Sun, Y. Lv, K. B. Schliep, Z. Zhao, J.-Y. Chen, P. M. Voyles, and J.-P. Wang, *Phys. Rev. Appl.* **9**, 044028 (2018).
- ¹⁹S. S. P. Parkin, N. More, and K. P. Roche, *Phys. Rev. Lett.* **64**, 2304 (1990).
- ²⁰Y.-J. Chang, A. Canizo-Cabrera, V. Garcia-Vazquez, Y.-H. Chang, and T. Wu, *J. Appl. Phys.* **113**, 17B909 (2013).
- ²¹S.-H. Yang, K.-S. Ryu, and S. Parkin, *Nat. Nanotechnol.* **10**, 221–226 (2015).
- ²²E. Liu, Y.-C. Wu, S. Couet, S. Mertens, S. Rao, W. Kim, K. Garello, D. Crotti, S. Van Elshocht, J. De Boeck, G. S. Kar, and J. Swerts, *Phys. Rev. Appl.* **10**, 054054 (2018).
- ²³M. Lavanant, P. Vallobra, S. Petit Watelot, V. Lomakin, A. D. Kent, J. Sun, and S. Mangin, *Phys. Rev. Appl.* **11**, 034058 (2019).
- ²⁴G. Mihajlović, N. Smith, T. Santos, J. Li, M. Tran, M. Carey, B. D. Terris, and J. A. Katine, *Phys. Rev. Appl.* **13**, 024004 (2020).
- ²⁵S. Watanabe, T. Komine, T. Kai, and K. Shiiki, *J. Magn. Magn. Mater.* **220**, 277 (2000).
- ²⁶D. M. Lattery, J. Zhu, D. Zhang, J.-P. Wang, P. A. Crowell, and X. Wang, *Appl. Phys. Lett.* **113**, 162405 (2018).
- ²⁷J. Zhu, X. Wu, D. M. Lattery, W. Zheng, and X. Wang, *Nanoscale Microscale Thermophys. Eng.* **21**, 177–198 (2017).
- ²⁸D. M. Lattery, D. Zhang, J. Zhu, X. Hang, J.-P. Wang, and X. Wang, *Sci. Rep.* **8**, 13395 (2018).
- ²⁹H. Shima, K. Oikawa, A. Fujita, K. Fukamichi, K. Ishida, and A. Sakuma, *Phys. Rev. B* **70**, 224408 (2004).
- ³⁰E. Yang, D. E. Laughlin, and J. G. Zhu, *IEEE Trans. Magn.* **48**, 7 (2012).
- ³¹K. Kusada, H. Kobayashi, R. Ikeda, Y. Kubota, M. Takata, S. Toh, T. Yamamoto, S. Matsumura, N. Sumi, K. Sato, K. Nagaoka, and H. Kitagawa, *J. Am. Chem. Soc.* **136**, 1864–1871 (2014).
- ³²M. Kobayashi, N. Ando, T. Kai, N. Takano, and K. Shiiki, *J. Phys.: Condens. Matter* **7**, 9607 (1995).
- ³³D. A. Gilbert, L.-W. Wang, T. J. Klemmer, J.-U. Thiele, C.-H. Lai, and K. Liu, *Appl. Phys. Lett.* **102**, 132406 (2013).
- ³⁴R. K. Dumas, Y. Fang, B. J. Kirby, C. Zha, V. Bonanni, J. Nogués, and J. Åkerman, *Phys. Rev. B* **84**, 054434 (2011).
- ³⁵P. He, X. Ma, J. W. Zhang, H. B. Zhao, G. Lüpke, Z. Shi, and S. M. Zhou, *Phys. Rev. Lett.* **110**, 077203 (2013).
- ³⁶D. Apalkov, S. Watts, A. Driskill-Smith, E. Chen, Z. Diao, and V. Nikitin, *IEEE Trans. Magn.* **46**, 2240–2243 (2010).
- ³⁷L. Thomas, G. Jan, S. Serrano-Guisan, H. Liu, J. Zhu, Y.-J. Lee, S. Le, J. Iwata-Harms, R.-Y. Tong, S. Patel, V. Sundar, D. Shen, Y. Yang, R. He, J. Haq, Z. Teng, V. Lam, P. Liu, Y.-J. Wang, T. Zhong, H. Fukuzawa, and P. Wang, in *Proceedings of the International Electron Devices Meeting Digest* (2018), pp. 27.3.1–27.3.4.
- ³⁸M. C. Hickey and J. S. Moodera, *Phys. Rev. Lett.* **102**, 137601 (2009).
- ³⁹Y. Tserkovnyak, A. Brataas, and G. E. W. Bauer, *Phys. Rev. Lett.* **88**, 117601 (2002).
- ⁴⁰E. Barati, M. Cinal, D. M. Edwards, and A. Umerski, *Phys. Rev. B* **90**, 014420 (2014).